Hindawi
Advances in Civil Engineering
Volume 2019, Article ID 1025483, 14 pages
https://doi.org/10.1155/2019/1025483

Research Article

IBIEM Analysis of Dynamic Response of a Shallowly Buried Lined Tunnel Based on Viscous-Slip Interface Model

Xiaojie Zhou,[1,2] **Qinghua Liang**,[1,2] **Zhongxian Liu**,[1,2] **and Ying He**[1,2]

[1]*Tianjin Key Laboratory of Civil Structure Protection and Reinforcing, Tianjin Chengjian University, Tianjin 300384, China*
[2]*School of Civil Engineering, Tianjin Chengjian University, Tianjin 300384, China*

Correspondence should be addressed to Zhongxian Liu; zhongxian1212@163.com

Received 10 September 2018; Accepted 30 January 2019; Published 6 March 2019

Guest Editor: Xihong Zhang

A viscous-slip interface model is proposed to simulate the contact state between a tunnel lining structure and the surrounding rock. The boundary integral equation method is adopted to solve the scattering of the plane SV wave by a tunnel lining in an elastic half-space. We place special emphasis on the dynamic stress concentration of the lining and the amplification effect on the surface displacement near the tunnel. Scattered waves in the lining and half-space are constructed using the fictitious wave sources close to the lining surfaces based on Green's functions of cylindrical expansion and the shear wave source. The magnitudes of the fictitious wave sources are determined by viscous-slip boundary conditions, and then the total response is obtained by superposition of the free and scattered fields. The slip stiffness and viscosity coefficients at the lining-surrounding rock interface have a significant influence on the dynamic stress distribution and the nearby surface displacement response in the tunnel lining. Their influence is controlled by the incident wave frequency and angle. The hoop stress increases gradually in the inner wall of the lining as sliding stiffness increases under a low-frequency incident wave. In the high-frequency resonance frequency band, where incident wave frequency is consistent with the natural frequency of the soil column above the tunnel, the dynamic stress concentration effect is more significant when it is smaller. The dynamic stress concentration factor inside the lining decreases gradually as the viscosity coefficient increases. The spatial distribution and the displacement amplitudes of surface displacement near the tunnel change as incident wave frequency and angle increase. The effective dynamic analysis of the underground structure under an actual strong dynamic load should consider the slip effect at the lining-surrounding rock interface.

1. Introduction

Analyses of seismic damage incurred by disasters such as the Kobe earthquake, Chi-Chi earthquake, and Wenchuan earthquake have shown that underground structures might be severely damaged during strong earthquakes, resulting in massive economic and societal losses [1–5]. As the scope and scale of modern underground structures continually increase, the seismic design grows increasingly complex. In theory, wave scattering and dynamic stress concentration effects should be considered for large underground structures during the seismic wave propagation process. To this effect, it is of great significance to study the seismic response and hazards feature of underground structures.

In general, the calculation methods include the analytical method [6–9], finite element method [10–12], finite difference method [13–15], boundary element method [16–19], boundary integral equation method [20–23], etc. It is worth mentioning that all of these studies assumed that the lining and surrounding rock are completely bonded. In actuality, however, there are varying degrees of slip between the tunnel and surrounding rock—especially in the case of intense dynamic loading. Yi et al. [24] studied the dynamic response of a tunnel lining with a sliding interface under an incident P wave based on an interface contact model. Fang and Jin [25, 26] proposed a viscoelastic interface model to solve the dynamic response of a tunnel lining under different interface stiffness and viscosity coefficients with incident P

and SV waves. Ping et al. [27] calculated the maximum moment and axial force of a circular shield tunnel under interface slip and no-slip states based on an equivalent stiffness circle.

It should be noted that the abovementioned research works based on interface contact models were mainly limited to deep-buried tunnels, while the response of shallow-buried tunnels differs significantly from that of deep-buried ones [28]. Yi et al. [29] presented an analytical solution to the out-of-plane dynamic response of a shallow tunnel lining under the action of a plane SH wave including interface contact stiffness, incident angle, wave frequency, and tunnel depth as these factors affect the dynamic stress concentration of the lining. Fang et al. [30] investigated a lined tunnel in a semi-infinite alluvial valley with an elastic-slip interface and analyzed the dynamic stress distribution around the circular tunnel subjected to SH waves.

However, until now, few studies have explored the seismic response of shallow tunnels under incident SV waves with the interface-slipping model due to the complexity of multimode coupling and hybrid boundary conditions. We used an indirect boundary integral equation method (IBIEM) to solve the scattering of the plane SV wave by a tunnel lining in a half-space based on the viscous-slip interface model. This method had been used effectively to solve the dynamic response of the tunnel structure [31, 32].

This study aims to investigate the dynamic stress concentration effect of the tunnel lining and the surface displacement amplification near the tunnel with a viscous-slip interface. We assessed the influence of parameters such as incident wave frequency and angle, viscous-slip interface stiffness, and viscosity coefficient on the overall dynamic response of the lining and surrounding rock. This study can provide a theoretical basis for the seismic design of actual underground engineering structures under intense dynamic loads.

2. Calculation Model

As shown in Figure 1, the elastic half-space contains an infinitely long tunnel lining. Both the lining and the half-space are linearly isotropic homogeneous elastic media. The viscous-slip state between the tunnel and the surrounding rock can be assumed to consist of a series of linear springs and dampers. The parameters related to the half-space and the tunnel are shown in Table 1.

Let the buried depth of the tunnel be d, the inner and outer radii of the lining be a_1 and a_2, and the inner and outer boundary surfaces of the lining be S_0 and S, respectively. Assume that the plane SV wave is incident at an angle θ_α from the half-space.

3. Calculation Method

In this study, we considered the cylindrical shear wave source in the half-space as the fundamental solution. The indirect boundary integral equation method and viscous-slip boundary condition were used to solve the scattering of plane waves by tunnel linings and the dynamic response around the tunnel lining [20].

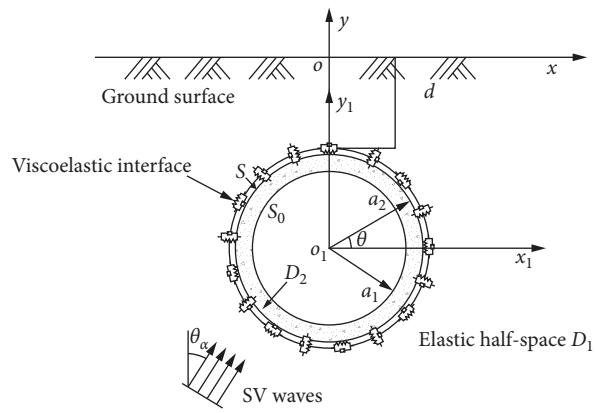

Figure 1: Seismic response model of tunnel lining with the viscous-slip interface.

3.1. Wave Field Analysis. The total half-space wave field can be viewed as a superposition of a half-space free field (without tunnel linings) and a scattering field. We first carry out a free field analysis. The shear wave potential function in the half-space is denoted as ψ (plane strain state), and the plane SV wave with circular frequency ω is incident at angle θ_α. In the Cartesian coordinate system, the incident SV wave potential function can be expressed as follows:

$$\psi^{(i)}(x, y) = \exp\left[-ik_{\alpha 1}\left(x \sin\theta_\alpha - y \cos\theta_\alpha\right)\right]. \quad (1)$$

For the sake of simplicity, the time factor $\exp(i\omega t)$ is omitted here. Incident plane SV waves generate reflected P waves and SV waves on the surface of the half-space. Their specific expressions are shown in [16].

Scattered fields are generated in the half-space of a lined tunnel and in the interior of the lining. The fields can be determined by superimposing all the expansion wave and shear wave sources on the virtual wave source surface inside and outside the lining, respectively. Assuming that the scattered field in the half-space is generated by the virtual source face S_1, the displacement and stress in the half-space are as follows:

$$u_i(x) = \int_b \left[b(x_1) G_{i,1}^{(s)}(x, x_1) + c(x_1) G_{i,2}^{(s)}(x, x_1)\right] dS_1,$$
$$\sigma_{ij}(x) = \int_b \left[b(x_1) T_{ij,1}^{(s)}(x, x_1) + c(x_1) T_{ij,2}^{(s)}(x, x_1)\right] dS_1, \quad (2)$$

where $x \in D_1$ and $x_1 \in S_1$. $b(x_1)$ and $c(x_1)$ correspond to the density of P and SV wave sources at the x_1 position on the virtual wave source surface S_1, respectively. $G_{i,l}^{(s)}(x, x_1)$ and $T_{ij,l}^{(s)}(x, x_1)$ denote Green's function of displacement and stress in the elastic half-space, respectively (lower scale index $l = 1$ or 2 corresponding to P and SV wave sources $i, j = x, y$), and function automatically satisfies the wave equation and surface boundary conditions.

Table 1: Half-space and tunnel parameters.

	Domain	Shear modulus	Poisson's ratio	Density	Longitudinal wave speed	Transverse wave speed	Virtual source surface
Half-space	D_1	μ_1	ν_1	ρ_1	$c_{\alpha 1}$	$c_{\beta 1}$	S_1
Tunnel	D_2	μ_2	ν_2	ρ_2	$c_{\alpha 2}$	$c_{\beta 2}$	S_2 and S_3

The internal scattering field of the lining is obtained by superimposing the action of all the expansion wave sources and shear wave sources on the virtual wave source surfaces S_2 and S_3. The internal displacement and stress of the lining are expressed as follows:

$$\begin{aligned} u_i(x) &= \int_b \left[d(x_2)G_{i,1}^{(l)}(x,x_1) + e(x_2)G_{i,2}^{(t)}(x,x_2)\right]dS_2 \\ &\quad + \int_b \left[f(x_3)G_{i,1}^{(t)}(x,x_3) + g(x_3)G_{i,2}^{(t)}(x,x_3)\right]dS_3, \\ \sigma_{ij}(x) &= \int_b \left[d(x_2)T_{ij,1}^{(s)}(x,x_2) + e(x_2)T_{ij,2}^{(t)}(x,x_2)\right]dS_2 \\ &\quad + \int_b \left[f(x_3)T_{ij,1}^{(t)}(x,x_3) + g(x_3)T_{ij,2}^{(t)}(x,x_3)\right]dS_3, \end{aligned} \tag{3}$$

where $x \in D_2$, $x_2 \in S_2$, and $x_3 \in S_3$. $d(x_2)$ and $e(x_2)$, respectively, correspond to the density of P and SV wave sources at the x_2 position on the virtual wave source surface S_2. $f(x_3)$ and $g(x_3)$ correspond to the density of P and SV wave sources at the x_3 position on the virtual wave source surface S_3. $G_{i,l}^{(t)}$ and $T_{ij,l}^{(t)}$ indicate the displacement and stress Green's functions in the lining, respectively.

The total displacement and stress fields in the half-space are obtained by superposition of the scattered wave field and the free field in the half-space. The internal reactions of the lining are all generated by the scattered fields within it.

3.2. Boundary Conditions and Solutions. We built a viscous-slip interface model to determine the influence of the interface effect on the dynamic response. The lining and the half-space were connected by linear springs and dampers (Figure 1). Spring and damper parameters are represented by stiffness and viscosity coefficients. In this model, the boundary conditions at the interface between the lining and the half-space (S) are as follows:

$$\begin{aligned} u_x^s - u_x^t &= \frac{\sigma_{nn}^s}{k_n} + \delta_n \frac{\partial(u_x^s - u_x^t)}{\partial t}, \quad (r = a_2), \\ u_y^s - u_y^t &= \frac{\sigma_{nt}^s}{k_t} + \delta_t \frac{\partial(u_y^s - u_y^t)}{\partial t}, \quad (r = a_2), \\ \sigma_{nn}^s &= \sigma_{nn}^t; \sigma_{nt}^s = \sigma_{nt}^t, \quad (r = a_2), \\ \sigma_{nn}^t &= 0; \sigma_{nt}^t = 0, \quad (r = a_1), \end{aligned} \tag{4}$$

where superscripts s and t correspond to the half-space and the lining, respectively; k_n and k_t are the normal and tangential stiffness coefficients of the viscous-slip boundary; and δ_n and δ_t are the normal and tangential viscosity coefficients of the viscous-slip boundary, respectively. To secure a numerical solution to the problem, we first discretely separate the inner and outer surfaces of the lining and the virtual wave source surfaces S_1, S_2, and S_3. The number of discrete points on the inner and outer surfaces of the lining is set to N, and the number of discrete points on the virtual wave source surfaces S_1, S_2, and S_3 is N_1. The scattered displacement and stress fields in the half-space can be expressed as follows:

$$\begin{aligned} u_i(x_n) &= b_{n1}G_{i,1}^{(s)}(x_n, x_{n1}) + c_{n1}G_{i,2}^{(s)}(x_n, x_{n1}), \\ \sigma_{ij}(x_n) &= b_{n1}T_{ij,1}^{(s)}(x_n, x_{n1}) + c_{n1}T_{ij,2}^{(s)}(x_n, x_{n1}), \end{aligned} \tag{5}$$

where $x_n \in S$ and $x_{n1} \in S_1$ ($n = 1, \ldots, N$ and $n1 = 1, \ldots, N_1$). b_{n1} and c_{n1} are the density of P wave and SV wave sources at the $n1$th discrete point on the virtual source surface S_1. Similarly, the scattering field inside the lining can be constructed from discrete wave sources on S_2 and S_3. The scattering displacement and stress fields are

$$\begin{aligned} u_i(x_n) &= d_{n2}G_{i,1}^{(t)}(x_n, x_{n2}) + e_{n2}G_{i,2}^{(t)}(x_n, x_{n2}) \\ &\quad + f_{n3}G_{i,1}^{(t)}(x_n, x_{n3}) + g_{n3}G_{i,2}^{(s)}(x_n, x_{n3}), \\ \sigma_{ij}(x_n) &= d_{n2}T_{ij,1}^{(t)}(x_n, x_{n2}) + e_{n2}T_{ij,2}^{(t)}(x_n, x_{n2}) \\ &\quad + f_{n3}T_{ij,1}^{(t)}(x_n, x_{n3}) + g_{n3}T_{ij,2}^{(t)}(x_n, x_{n3}), \end{aligned} \tag{6}$$

where $x_n \in S$, $x_{n2} \in S_2$, and $x_{n3} \in S_3$ ($n = 1, \ldots, N$, $n2 = 1, \ldots, N_1$, and $n3 = 1, \ldots, N_1$).

A linear system of equations can be obtained by synthesizing the above formulas:

$$\begin{aligned} (W_1 + B_1)Y_1 + F &= (W_2 + B_2)Y_2 + (W_3 + B_3)Y_3, \\ H_1Y_1 + F &= H_2Y_2 + H_3Y_3, \\ T_2Y_2 + T_3Y_3 &= 0, \end{aligned} \tag{7}$$

where W_1, W_2, and W_3 are the displacement Green's influence matrix of the discrete points on the outer surface of the lining of the discrete wave source on S_1, S_2, and S_3, respectively; B_1, B_2, and B_3 are boundary displacement matrices obtained from boundary conditions; H_1, H_2, and H_3 are the stress Green's influence matrix of the discrete points on the outer surface of the lining of discrete source points on S_1, S_2, and S_3, respectively; T_2 and T_3 correspond to the stress-green-influenced matrix of the discrete points on the inner surface of the lining of the source points of S_2 and S_3; Y_1, Y_2, and Y_3 are the virtual wave source density vectors (to be determined) on S_1, S_2, and S_3, respectively; and F is the free field vector. System (7) can be solved using the least-squares method. The virtual wave source density is obtained, and then the scattered field is obtained. The total wave field can be obtained by superimposing the scattering

field and the free field, and then the displacement and stress of the half-space and any point in the lining can be calculated.

4. Numerical Example and Validation

In this section, the ratio of the buried depth of the tunnel to the inner radius of the lining is $d/a_1 = 1.0$; the ratio of the inner and outer radii of the lining is $a_1/a_2 = 0.9$. Poisson's ratios ν of the half-space and the lining material are both 0.25. The material's hysteretic damping ratio is 0.001, and the density ratio of the half-space and lining material is $\rho_1/\rho_2 = 0.8$. The ratio of the shear wave speed in the half-space and the lining is $c_{\beta 1}/c_{\beta 2} = 0.2$. We define η as the dimensionless incident frequency $\eta = 2a_1/\lambda_1 = \omega a_1/\pi c_{\beta 1}$. η represents the ratio of the inner diameter of the tunnel to the half-space shear wavelength.

We define the dimensionless dynamic stress concentration factor (DSCF) as DSCF $= |\sigma_{\theta\theta}/\sigma_0| = |\sigma_{\theta\theta}/\mu k_{\beta 1}^2|$. DSCF represents the absolute value of the ratio of the circumferential stress $\sigma_{\theta\theta}$ of the lining hole to the amplitude σ_0 of the incident wave stress in the half-space; k^* is the dimensionless stiffness factor of the viscous-slip interface, and $k^* = k_n a_1/\mu_1 = k_t a_1/\mu_1$; and δ^* is the dimensionless viscosity factor of the viscous-slip interface, and $\delta^* = \delta_t/a_1 = \delta_n/a_1$. In this paper, the dimensionless stiffness factor k^* is 1, 5, 10, and 20, respectively. The dimensionless viscosity factor δ^* is 0. We found that the interface is essentially in a no-slip state when k^* exceeds 20, so when the stiffness factor exceeds 20, we specify the interface is the no-slip state.

In order to verify the correctness of the IBIEM method, we first let k^* be 100 and δ^* be 0, which is equivalent to the state of consolidation without slip, and then compare it with the state of no slip in [20]. To more fully prove the accuracy, we choose the spectrum analysis of the different locations of the lining and compare them with [20]. The calculation positions are at $\theta = 90^\circ$ (the top of the lining), 45°, 0°, −45°, and −90° (the bottom of the lining), respectively, as shown in Figure 2. The DSCF of $\theta = 90^\circ$ (the top of the lining) and −90° (the bottom of the lining) is 0, so it is not shown in Figure 2. As shown in Figure 2, the results calculated by the IBIEM method are quite consistent with the results in [20]. This proves the correctness of our calculation method.

5. Numerical Analysis

5.1. DSCF of Inner and Outer Lining Wall Surfaces under Single-Frequency Incident Wave

5.1.1. Influence of Stiffness Factor k^*. Figures 3–6 show the distribution of DSCF in the inner and outer wall of a rigid lining under an incident SV wave. Among them, the dimensionless incident frequency η is 0.25, 0.5, 1, and 2, respectively. The incidence angle θ_α is 0° and 30°, respectively;

As shown in Figures 3–6, under an incident plane SV wave, the DSCF distribution curves of inner and outer wall surfaces of the lining are similar. The inner wall stress amplitude is considerably larger than that of the outer wall. When the SV wave is incident at low frequency ($\eta = 0.25$, 0.5), the DSCF of the inner lining wall surface increases as the stiffness factor k^* increases while the DSCF of the outer wall decreases as k^* increases. When $\eta = 0.5$ and $\theta_\alpha = 0^\circ$, k^* is either 1, 5, 10, or 20; the DSCF of the outer wall surface is, respectively, 23.79, 23.04, 21.45, and 19.91.

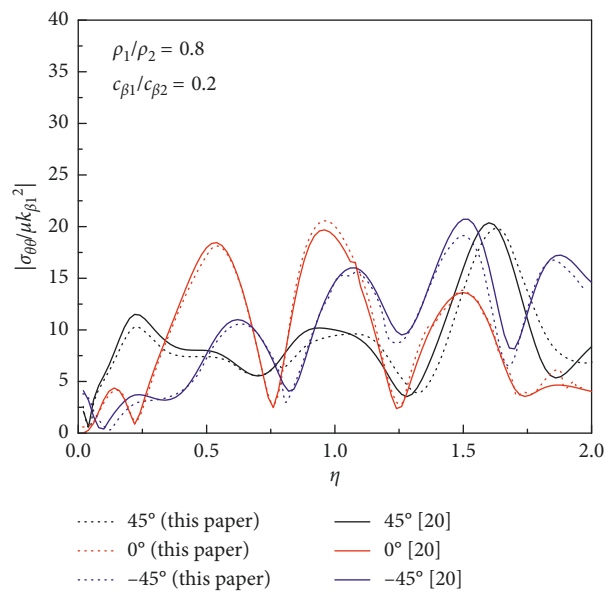

Figure 2: DSCF spectrum distribution on the inner lining wall surface.

When the SV wave is obliquely incident, the increase and decrease amplitudes of the DSCF of the inner and outer wall surfaces is smaller than the normal incidence. When $\eta = 0.25$, $\theta_\alpha = 0^\circ$, and $k^* = 1$, the DSCF of the inner wall surface is 51.71. It is 58.39 when $k^* = 20$ marking an increase in amplitude of 13%. When $k^* = 1$, the DSCF of the outer wall surface is 37.21, corresponding to 16.26 when $k^* = 20$, and the amplitude of increase is 56%. When $\eta = 0.25$, $\theta_\alpha = 30^\circ$, and $k^* = 1$, the DSCF of the inner wall surface is 46.74 and it corresponds to 50.34 when $k^* = 20$, and the increase in amplitude is 8%. When $k^* = 1$, the DSCF of the outer wall surface is 28.64, corresponding to 20.15 when $k^* = 20$ at a decrease in amplitude of 30%.

When SV wave is incident with frequency $\eta = 1$, the DSCF of the inner and outer wall of the lining decreases with the increase of k^*, and the dynamic stress concentration on the inner and outer wall surfaces is very significant when $k^* = 1$. If the SV wave is obliquely incident, the DSCF of the inner wall surface is to 69.60 when $k^* = 1$, which is 2.1 times as much as the peak 32.93 under $k^* = 20$. The peak DSCF of the outer wall surface is 60.36, which is 2.8 times as much as the corresponding peak value 21.92 under $k^* = 20$. The SV wave is inclined at an angle of 30°; the peak DSCF on the inner wall of the lining is 67.78 when $k^* = 1$, which is 2.3 times as much as the peak 29.62 under $k^* = 20$. Section 3.2 discusses this phenomenon in detail.

When the SV wave is incident at high frequency ($\eta = 2$), the DSCF curve on the inner and outer wall surfaces of the lining oscillates very sharply along the circumference of the hole. There is no obvious relationship between the vibration regularity and k^*. When the SV wave is inclined at an

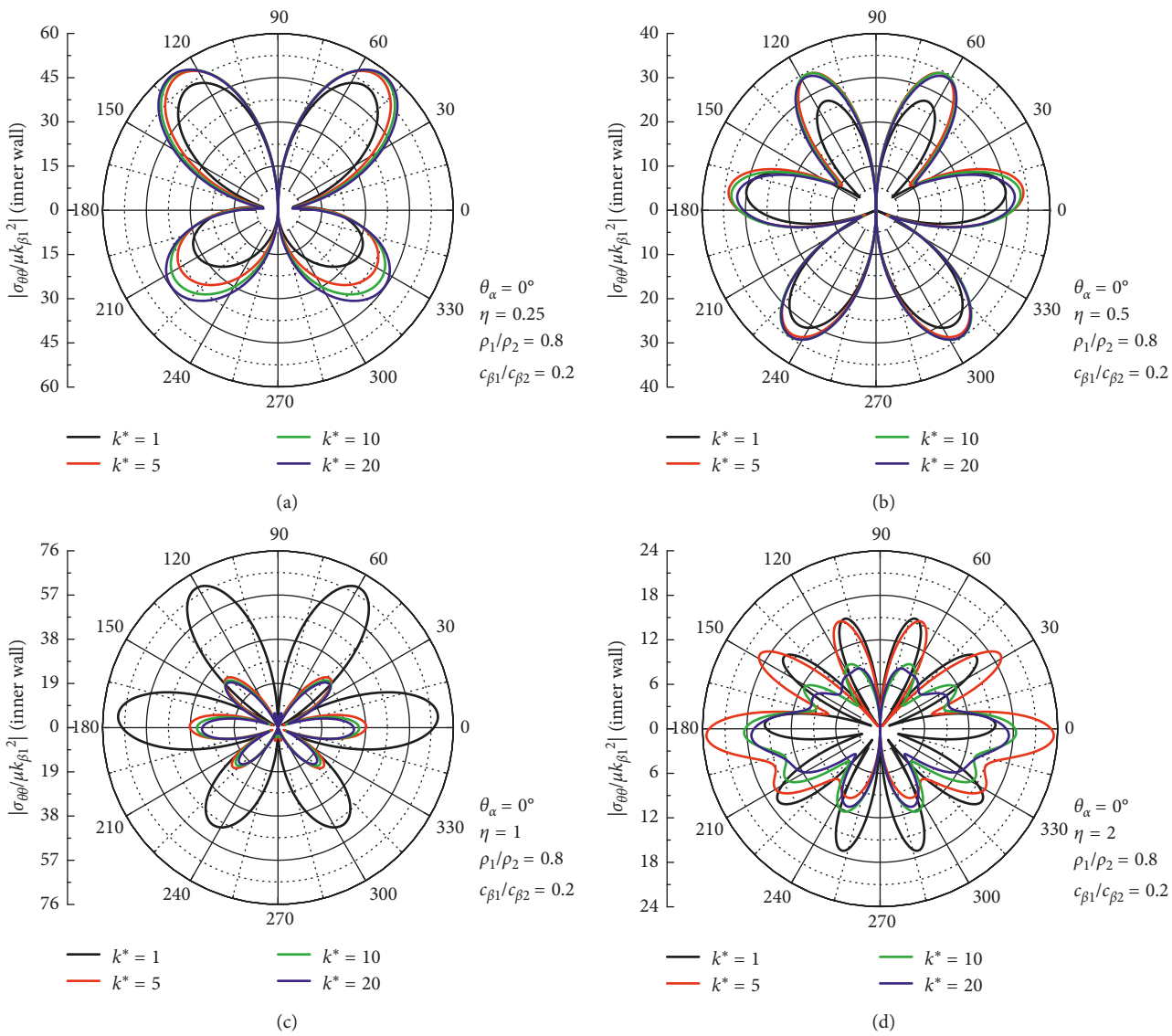

Figure 3: DSCF distribution on lining the inner wall under the incident SV wave ($\theta_\alpha = 0°$): (a) $\eta = 0.25$; (b) $\eta = 0.5$; (c) $\eta = 1$; (d) $\eta = 2$.

incidence of 30°s and $k^* = 1$, the DSCF of the inner and outer wall surfaces is minimal: the peak value of the inner wall falls to 12.64. When $k^* = 20$, the peak values of the hoop stress of the inner and outer wall surfaces are 27.50 and 23.26, respectively.

5.1.2. Influence of Viscosity Factor δ^*. Figure 7 shows the distribution of DSCF of the outer lining wall surface under an incident SV wave. The dimensionless incident frequency η is 0.25, 0.5, and 1, respectively; the incident angle θ_α is 0° and 30°, respectively. The dimensionless stiffness factor $k^* = 5$, and the viscosity factor δ^* is 1, 10, or 100.

As shown in Figure 7, the DSCF of the outer wall of the lining decreases gradually as interfacial viscosity factor δ^* increases. However, the influence of the viscosity factor δ^* on the circumferential stress distribution of the lining gradually weakens as incident wave frequency increases. For example, when the SV wave is of low frequency ($\eta = 0.25$) at normal incidence, the DSCF of the outer wall is 27.32 when $\delta^* = 1$, that is, 2.3 times the corresponding value of 11.90 when $\delta^* = 10$ and 2.6 times the corresponding value of 10.43 when $\delta^* = 100$. The SV wave is under $\eta = 1$ at normal incidence. The DSCF of the outer wall is 25.56 when $\delta^* = 1$, 1.35 times the corresponding value of 18.93 when $\delta^* = 10$, and 1.39 times the corresponding value of 18.43 when $\delta^* = 100$.

Compared to the normal incidence, the influence of the viscosity factor on the amplitude distribution of the circumferential stress of the lining weakens at oblique incidence. When the SV wave is incident at an angle of 30°, the spatial distribution of the circumferential stress of the lining is relatively gentle along the circumference of the hole. In the low-frequency region ($\eta = 0.25$), when $\delta^* = 1$, the DSCF of the outer wall is 23.99, which is equal to 1.3 times the value of 18.23 when $\delta^* = 100$. When $\eta = 1$ and $\delta^* = 1$, the DSCF of the outer wall of the lining is 27.12, which is 1.1 times the corresponding value of 23.60 when $\delta^* = 100$.

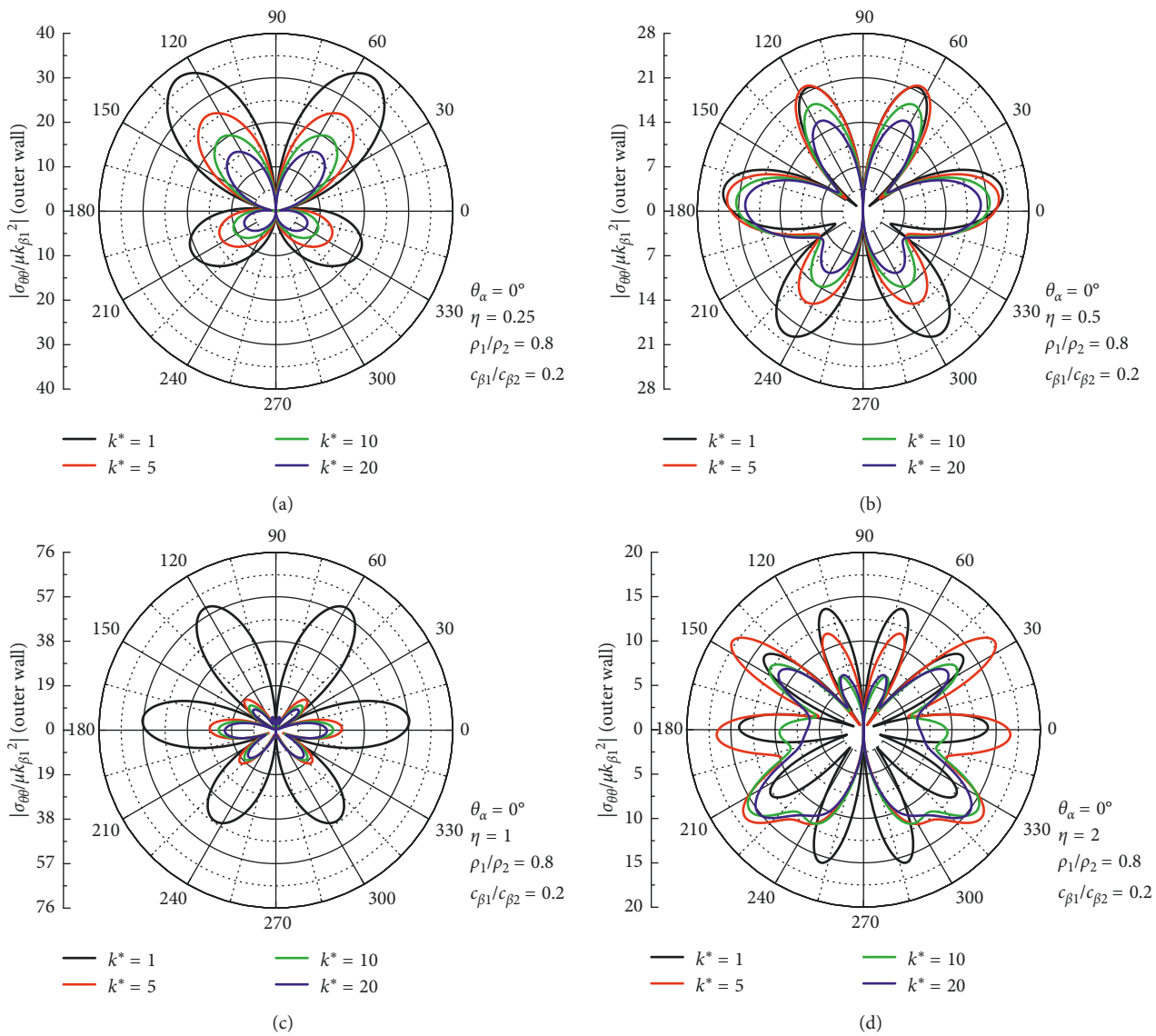

Figure 4: DSCF distribution on lining the outer wall under the incident SV wave ($\theta_\alpha = 0°$): (a) $\eta = 0.25$; (b) $\eta = 0.5$; (c) $\eta = 1$; (d) $\eta = 2$.

5.2. Lining Internal DSCF Spectrum Analysis. Figures 8 and 9 show the influence of the dimensionless stiffness factor k^* on the DSCF at different positions of the inner and outer walls of the tunnel lining when the SV wave is perpendicularly incident in the spectrum state, and the viscosity factor δ^* is 0. Calculation positions were same as in Section 3, and the DSCF of $\theta = 90°$ (the top of the lining) and $-90°$ (the bottom of the lining) is not shown in Figures 8 and 9. Similar to our observations in the model without slipping, the stress of the lining is sensitive to changes in frequency. The spectrum curve also has obvious peaks and troughs. The peak frequency here corresponds to the natural frequency in the soil column above the lining [33].

As shown in Figure 8, under an SV wave with normal incidence, the interface slip stiffness factor k^* significantly affects the internal stress spectrum of the lining. When $k^* = 1$, the stress amplification effect in the resonance reaction section is particularly obvious. At the first-order resonance frequency ($\eta = 0.16$), the stress peak at $\theta = 45°$ reaches 70.0; and at the $\eta = 0.96$ resonance frequency, the stress at $\theta = 0°$ has a peak of 77.2. The stress peak in the resonance band gradually decreases as the stiffness factor k^* gradually increases. For example, when $k^* = 20$ (near the no-slip state), the stress peaks at the first two resonance frequencies at $\theta = 45°$ are approximately 63.4 and 34.0. When the stiffness factor is small, the restraining effect of the lining on the upper soil column weakens and the response amplitude of the lining-upper soil column system in the resonant state is rather large, causing an increase in the corresponding stress amplitude.

The resonance frequency point also is offset to a certain extent as the sliding stiffness factor increases. When k^* is 1, 5, and 10, the first-order resonance frequency is 0.16, 0.18, and 0.20, respectively. This is due to the fact that the overall stiffness of the soil column above the lining increases as slip stiffness factor increases, and the stress spectrums of $k^* = 10$

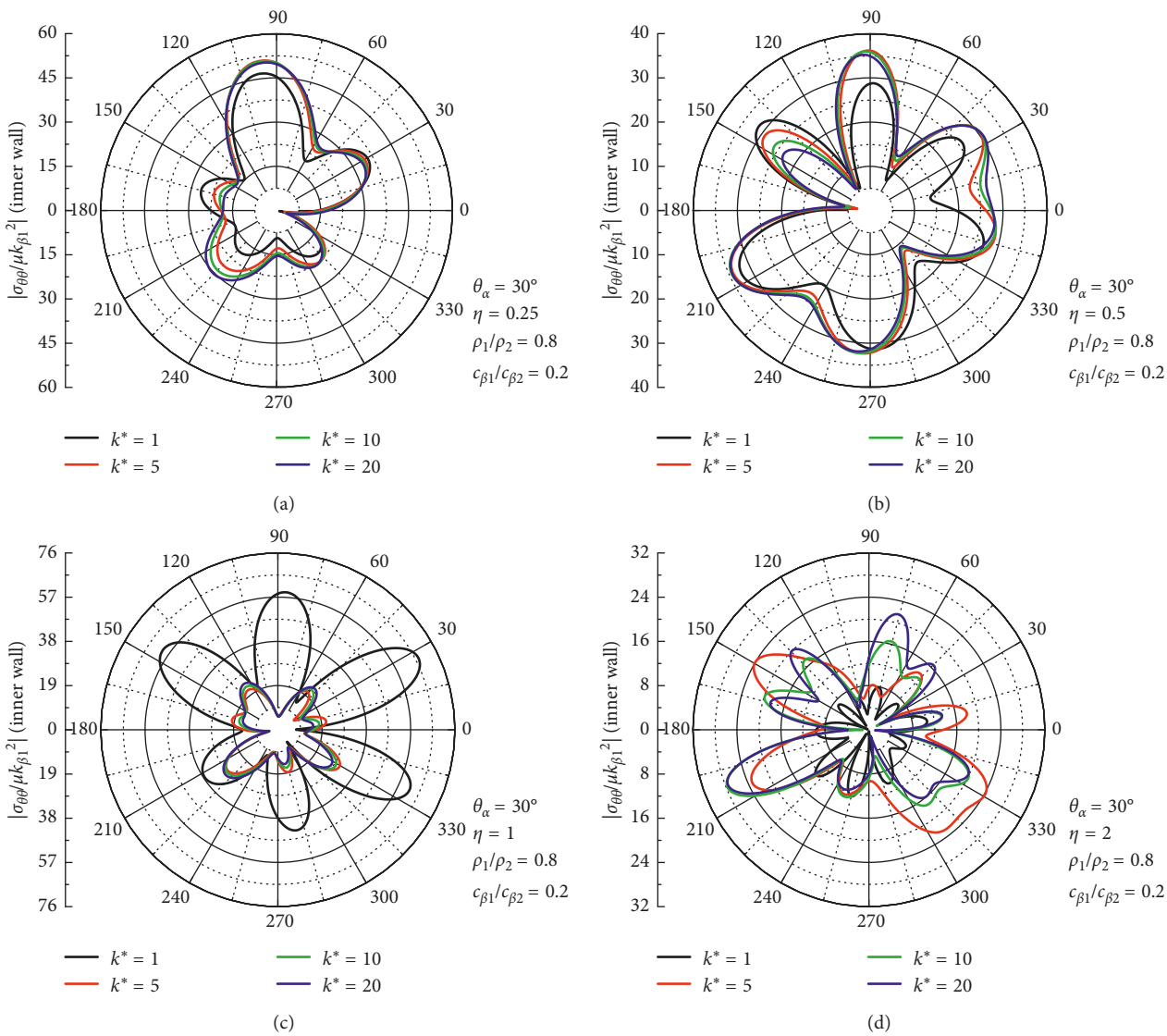

Figure 5: DSCF distribution on lining the inner wall under the incident SV wave ($\theta_\alpha = 30°$): (a) $\eta = 0.25$; (b) $\eta = 0.5$; (c) $\eta = 1$; (d) $\eta = 2$.

and $k^* = 20$ are similar. According to the spatial distribution, the stress spectrum curves at several typical observation points markedly differ. If the stress peak at $\theta = 45°$ occurs at the first-order natural frequency, the stress peak at $\theta = 0°$ occurs at the second-order natural frequency.

As shown in Figure 9, the frequency variation rule of the DSCF spectrum curve of the outer wall is similar to that of the inner wall, but the outer wall DSCF spectrum is generally smaller than the inner wall. When k^* is 1, 5, 10, and 20, the peaks of the inner wall DSCF reach 77.24, 65.65, 64.05, and 63.44 while the peaks of the outer wall DSCF are 64.14, 29.14, 24.87, and 22.33, respectively.

Figure 10 shows the DSCF spectrum of the outer wall surface of the lining based on the influence of the interfacial viscosity factor δ^*, where the peak of the DSCF spectrum of the outer wall decreases as the viscosity factor δ^* increases. When δ^* is 1, 10, and 100, the DSCF peaks are 30.43, 21.10, and 20.57, respectively. Increase in the viscosity factor δ^* causes greater energy loss during the sliding process, which in turn causes the DSCF of the lining surface to attenuate.

5.3. Displacement Amplitude of Ground Surface. Figures 11 and 12 show the surface displacement amplitude distribution above the tunnel lining as-affected by interface slip stiffness factor k^* under an incident SV wave. The surface displacement amplitude in the figure was standardized according to the displacement amplitude of the incident wave. The dimensionless incident frequency η is 0.25 and 0.5; the incident angle θ_α is 0° and 30°, and the dimensionless slip stiffness factor k^* is 1, 2, 10, and 20. The interface viscosity factor δ^* is 0.

Figures 11 and 12 show that when the SV wave has low frequency ($\eta = 0.25$) at normal incidence, the spatial distribution of surface displacement is basically consistent under different slip stiffness. The variations in the stiffness factor k^* have a considerable influence on the horizontal and

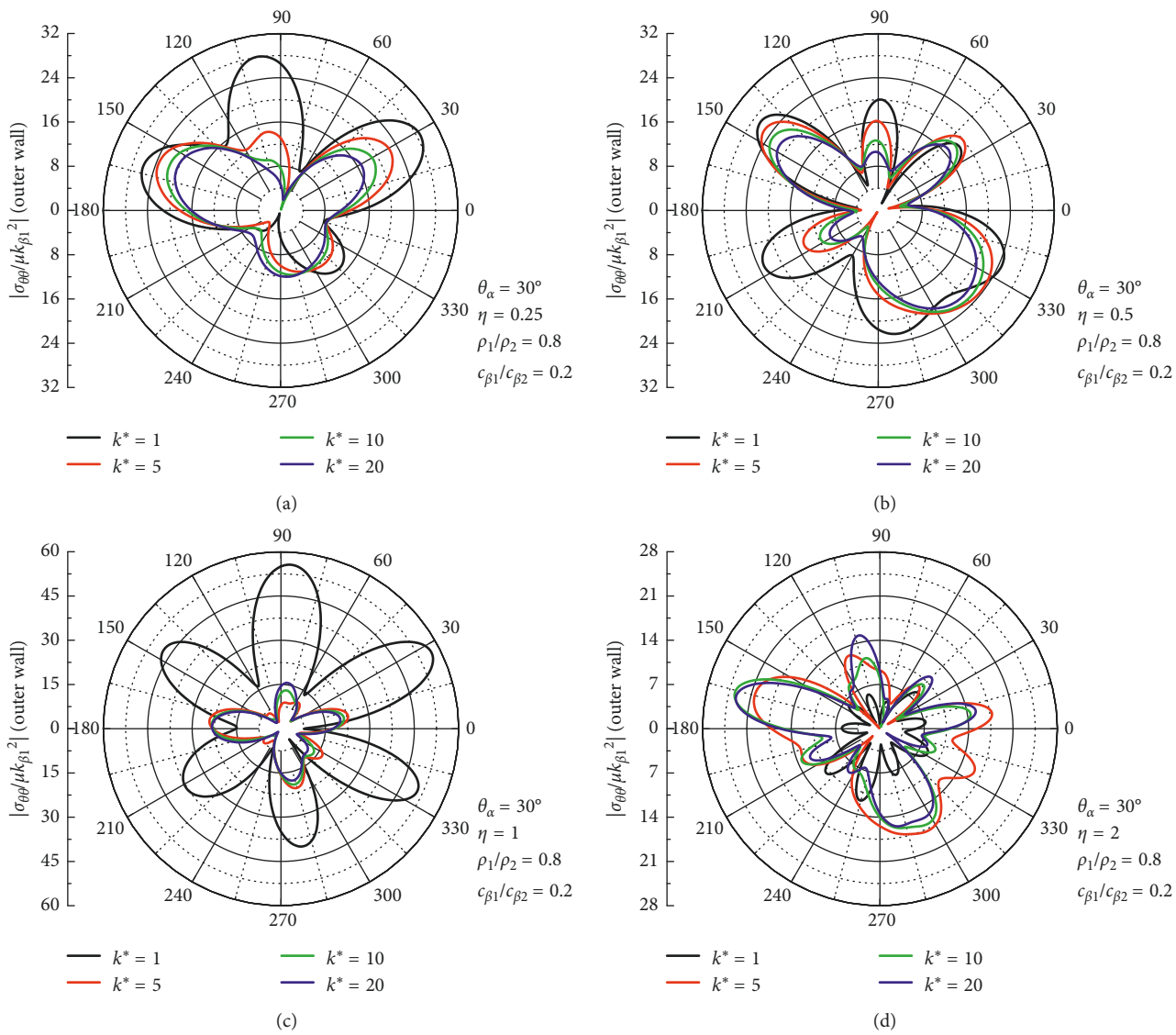

Figure 6: DSCF distribution on lining the outer wall under the incident SV wave ($\theta_\alpha = 30^\circ$): (a) $\eta = 0.25$; (b) $\eta = 0.5$; (c) $\eta = 1$; (d) $\eta = 2$.

vertical displacement amplitudes of the ground surface near the lining. The standard amplitude $|U_x/A_{sv}|$ of the horizontal displacement above the tunnel lining increases, while the standard amplitude $|U_y/A_{sv}|$ as k^* increases. The surface horizontal displacement amplitudes at $k^* = 1$, 5, 10, and 20 were 2.04, 2.23, 2.29, and 2.32, respectively, while the vertical displacement amplitudes were 1.71, 1.41, 1.27, and 1.16, respectively.

When the SV wave is incident at an angle of 30° and at a low frequency ($\eta = 0.25$), any change in slip stiffness factor k^* has little effect on the horizontal displacement above the tunnel lining surface but does influence the spatial distribution and amplitude of the vertical displacement. The influence of k^* gradually increases as the incident frequency of the SV wave increases ($\eta = 0.5$) while the spatial distribution and amplitude of the lining's surface displacement also markedly change. The 30° oblique incidence has more significant effects than the normal incidence. Take the vertical incidence of the SV wave (Figure 12(a)) as an example: at the position of the lining directly above the surface (i.e., $x = 0$), the horizontal displacement amplitude of the surface decreases as k^* increases. The amplitude is 1.47 when $k^* = 1$, and the corresponding values for $k^* = 5$, 10, and 20 are 1.16, 1.05, and 0.98, respectively. Just above the two sides, the horizontal displacement amplitude increases as k^* increases.

6. Conclusion

The boundary integral equation method was applied to solve the seismic response of a tunnel lining in an elastic half-space under incident plane SV waves based on a viscous-slip interface model. The effects of key factors such as incident wave frequency and angle, interface slip stiffness, and interfacial viscosity coefficient on the dynamic stress response of the tunnel lining in elastic half-space and the surface displacement near the tunnel lining were analyzed. Main conclusions can be summarized as follows:

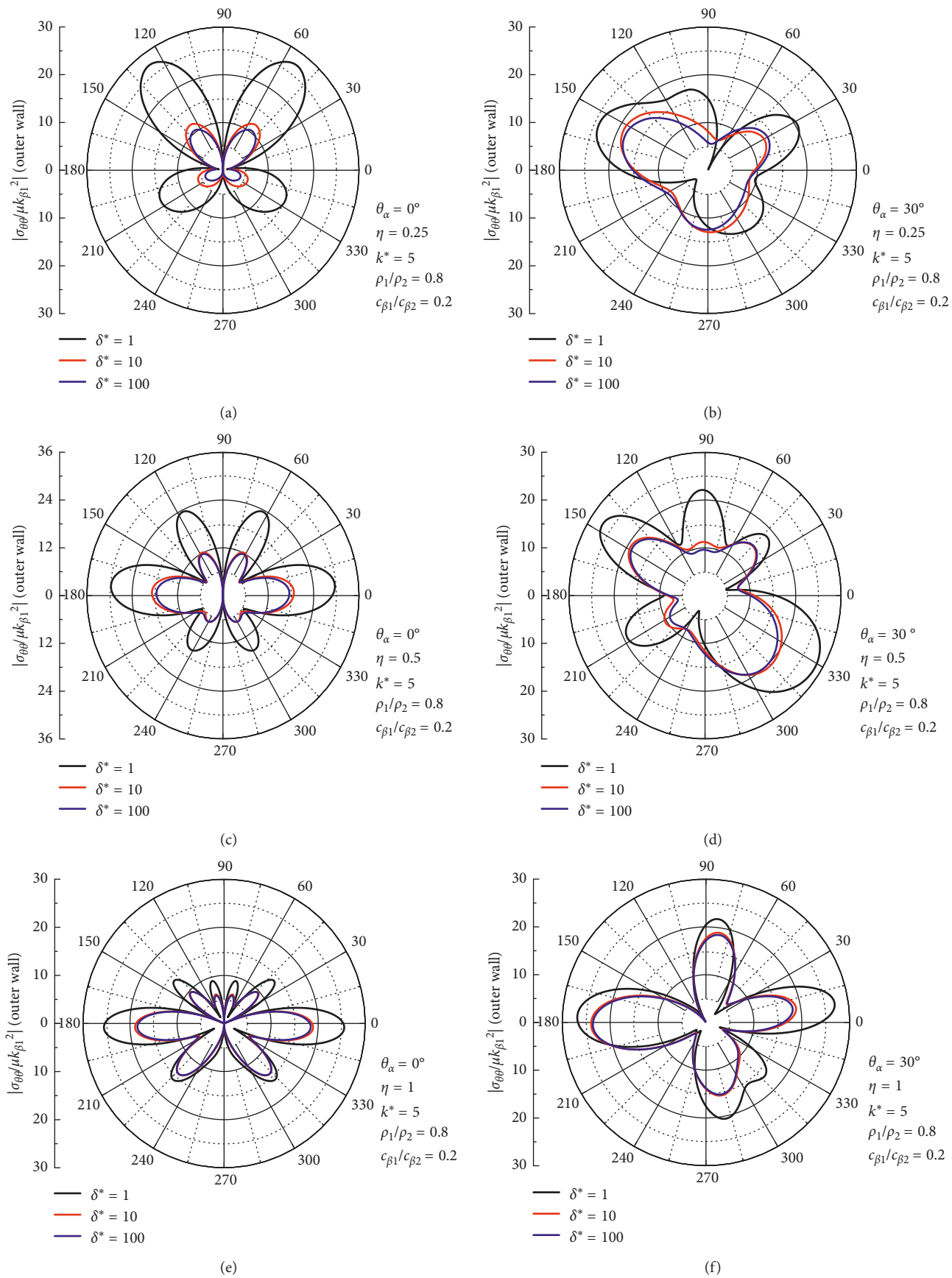

Figure 7: DSCF distribution on outer lining wall surfaces under incident SV waves: (a)$\eta = 0.25$, $\theta_\alpha = 0°$; (b) $\eta = 0.25$, $\theta_\alpha = 30°$; (c) $\eta = 0.5$, $\theta_\alpha = 0°$; (d) $\eta = 0.5$, $\theta_\alpha = 30°$; (e) $\eta = 1$, $\theta_\alpha = 0°$; (f) $\eta = 1$, $\theta_\alpha = 30°$.

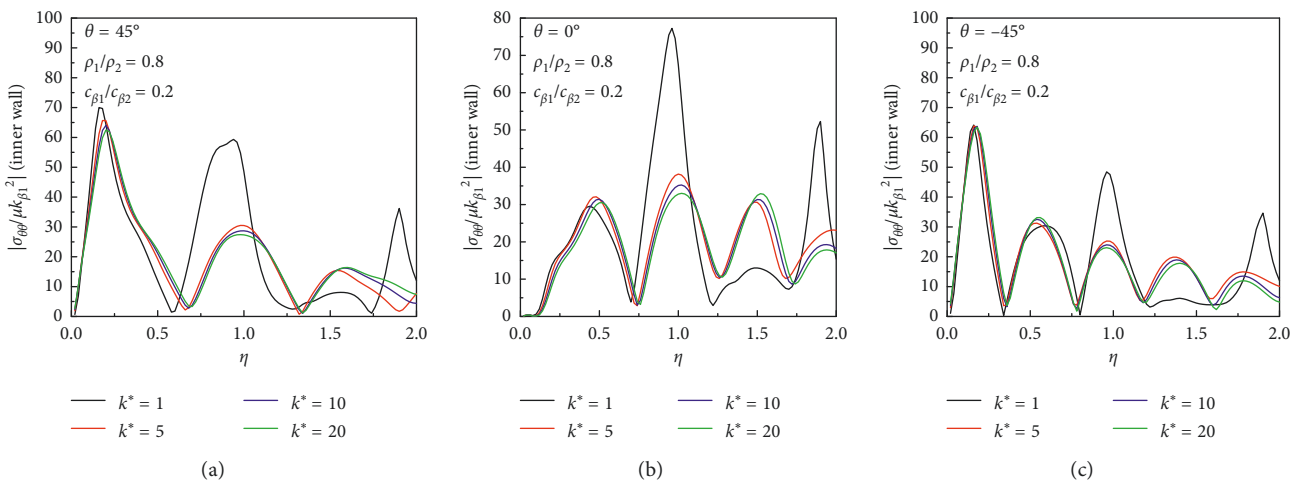

Figure 8: DSCF spectrum distribution on the inner lining wall surface under the vertically incident SV wave: (a) $\theta = 45^\circ$; (b) $\theta = 0^\circ$; (c) $\theta = -45^\circ$.

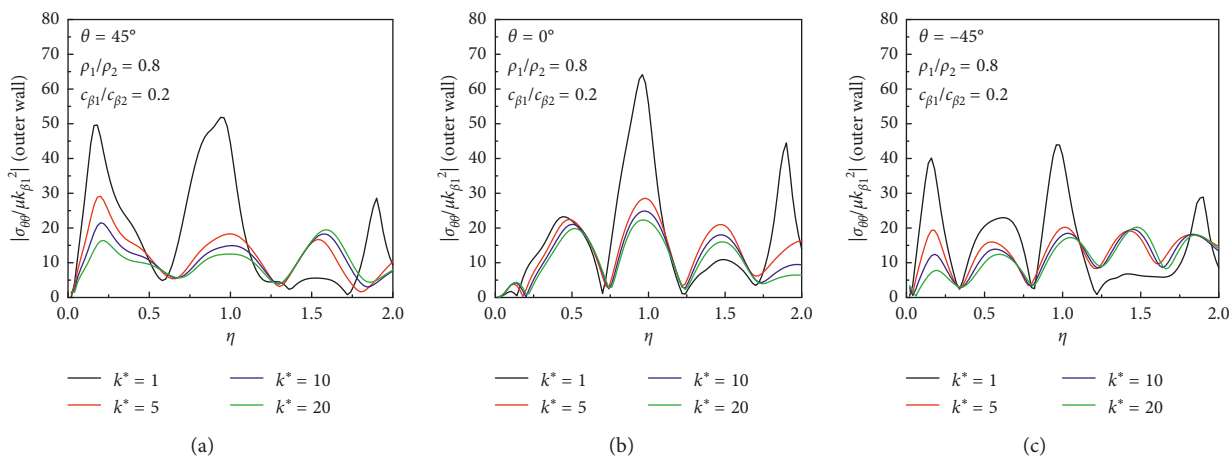

Figure 9: DSCF spectrum distribution on the outer lining wall surface under the vertically incident SV wave: (a) $\theta = 45^\circ$; (b) $\theta = 0^\circ$; (c) $\theta = -45^\circ$.

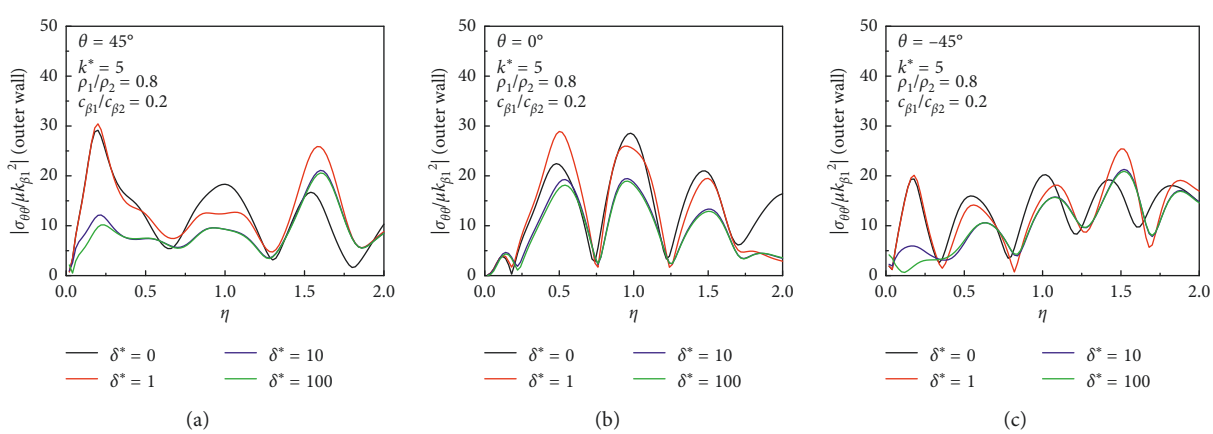

Figure 10: DSCF spectrum distribution on the outer lining wall surface under the vertically incident SV wave ($\delta^* = 0$, 1, 10, and 100): (a) $\theta = 45^\circ$; (b) $\theta = 0^\circ$; (c) $\theta = -45^\circ$.

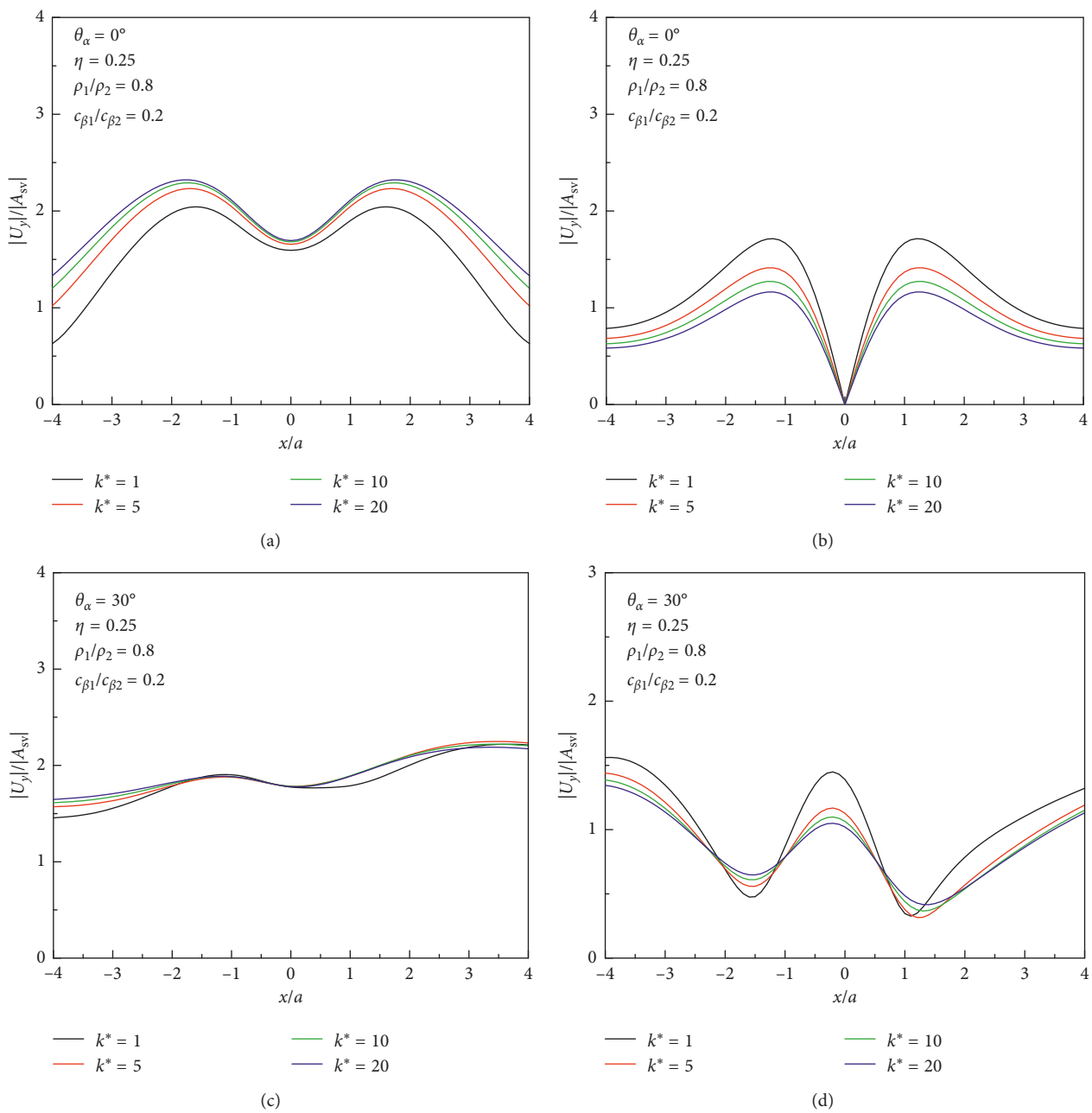

Figure 11: Surface displacement amplitudes near tunnel lining under the incident SV wave ($\eta = 0.25$): (a) surface horizontal displacement amplitude; (b) surface vertical displacement amplitude; (c) surface horizontal displacement amplitude; (d) surface vertical displacement amplitude.

(1) The interface slip stiffness factor significantly affects the dynamic stress distribution of the tunnel lining; the response characteristics are controlled by the incident wave frequency. When the slip stiffness is small, the internal stress of the lining changes very radically along the space around the hole, and the spatial distribution of the dynamic stress is highly complex. When the slip stiffness is large ($k^* \geq 20$), the dynamic response is close to that of the nonslip model.

Under an incident low-frequency wave, increase in interface slip stiffness causes a gradual increase in the circumferential stress of the inner wall. The dynamic stress concentration is more significant in the no-slip state than the slip state. When the SV wave is incident with $\eta = 1$ (close to the high-frequency resonant frequency band), the dynamic stress concentration effect inside the lining is very significant when the interface slip stiffness coefficient is small ($k^* = 1$). Under high-frequency wave incidence ($\eta = 2$), the influence of slip stiffness coefficient on the dynamic stress of the lining is more complex and spatial oscillation of the dynamic stress is more severe.

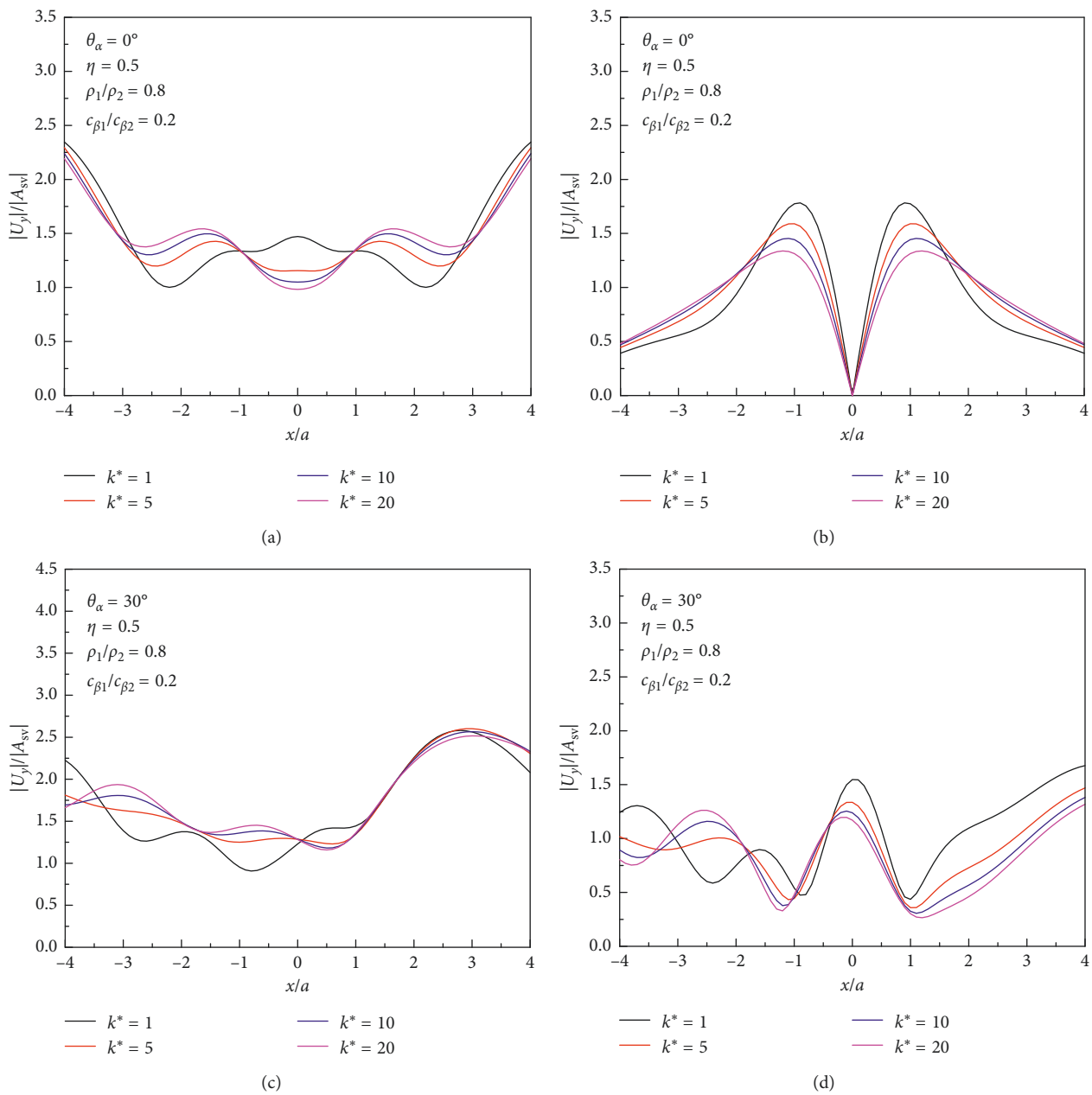

Figure 12: Surface displacement amplitude near tunnel lining under the incident SV wave ($\eta = 0.5$): (a) surface horizontal displacement amplitude; (b) surface vertical displacement amplitude; (c) surface horizontal displacement amplitude; (d) surface vertical displacement amplitude.

(2) The viscosity factor of the viscous-slip interface also has a significant influence on the dynamic stress distribution of the tunnel lining. As the viscosity factor increases, the DSCF of the lining outer wall decreases gradually; however, this effect gradually weakens as the incident wave frequency increases. The influence of the viscosity coefficient under a normally incident plane SV wave is greater than that under a wave with oblique incidence.

(3) The interface slip stiffness factor has a significant effect on the DSCF spectrum characteristics of the tunnel lining surface. When the slip stiffness is small ($k^* = 1$), the dynamic stress amplification effect in the high-frequency resonance reaction section is more obvious. The stress peak in the resonance band gradually decreases as the slip stiffness increases. The resonance frequency point is also offset to a certain extent as slip stiffness increases.

(4) When the SV wave is incident at a low frequency, the spatial distribution of surface displacements above the lining under different slip stiffness is essentially constant, but the displacement amplitudes are quite different. Any increase in SV wave incident frequency and incidence angle has a significant effect on

both the spatial distribution of surface displacement near the lining and the amplitude of said surface displacement.

In this study, we analyzed only the 2D seismic response of a shallow lined tunnel based on the viscous-slip interface model of a uniform space in half-space. Similar seismic response analyses of uneven sites and 3D tunnels merit further research.

Data Availability

The data used to support the findings of this study are included within the article.

Conflicts of Interest

The authors declare that they have no conflicts of interest.

Acknowledgments

The research described in this paper was financially supported by the National Natural Science Foundation of China under grant nos. 51678389 and 51678390 and the National Basic Research Program of China under grant no. 2015CB058002.

References

[1] Ö. Aydan, Y. Ohta, M. Geniş, N. Tokashiki, and K. Ohkubo, "Response and stability of underground structures in rock mass during earthquakes," *Rock Mechanics and Rock Engineering*, vol. 43, no. 6, pp. 857–875, 2010.

[2] Y. M. A. Hashash, J. J. Hook, B. Schmidt, and J. I.-C. Yao, "Seismic design and analysis of underground structures," *Tunnelling and Underground Space Technology*, vol. 16, no. 4, pp. 247–293, 2001.

[3] K. Uenishi and S. Sakurai, "Characteristic of the vertical seismic waves associated with the 1995 hyogo-ken nanbu (kobe), Japan earthquake estimated from the failure of the daikai underground station," *Earthquake Engineering and Structural Dynamics*, vol. 29, no. 6, pp. 813–821, 2015.

[4] I. Arango, "Theme paper: earthquake engineering for tunnels and underground structures," in *Proceedings of a Case History. Geotechnical Earthquake Engineering and Soil Dynamics Congress IV*, pp. 1–34, Sacramento, CA, USA, May 2011.

[5] Y. M. A. Hashash, D. Park, and J. I.-C. Yao, "Ovaling deformations of circular tunnels under seismic loading, an update on seismic design and analysis of underground structures," *Tunnelling and Underground Space Technology*, vol. 20, no. 5, pp. 435–441, 2005.

[6] K. A. Kuo, H. E. M. Hunt, and M. F. M. Hussein, "The effect of a twin tunnel on the propagation of ground-borne vibration from an underground railway," *Journal of Sound and Vibration*, vol. 330, no. 25, pp. 6203–6222, 2012.

[7] J. A. Forrest and H. E. M. Hunt, "A three-dimensional tunnel model for calculation of train-induced ground vibration," *Journal of Sound and Vibration*, vol. 294, no. 4-5, pp. 678–705, 2006.

[8] Q. Liu and R. Wang, "Dynamic response of twin closely-spaced circular tunnels to harmonic plane waves in a full space," *Tunnelling and Underground Space Technology*, vol. 32, no. 6, pp. 212–220, 2012.

[9] Y. Gao, D. Dai, N. Zhang et al., "Scattering of plane and cylindrical SH waves by a horseshoe shaped cavity," *Journal of Earthquake and Tsunami*, vol. 11, no. 2, article 1650011, 2016.

[10] A. Tateishi, "A study on seismic analysis methods in the cross section of underground structures using static finite element method," *Structural Engineering/Earthquake Engineering*, vol. 22, no. 1, pp. 41s–54s, 2005.

[11] H. Huo, A. Bobet, G. Fernández, and J. Ramírez, "Load transfer mechanisms between underground structure and surrounding ground: evaluation of the failure of the daikai station," *Journal of Geotechnical and Geoenvironmental Engineering*, vol. 131, no. 12, pp. 1522–1533, 2005.

[12] G. P. Kouretzis, G. D. Bouckovalas, and C. J. Gantes, "3-d shell analysis of cylindrical underground structures under seismic shear (s) wave action," *Soil Dynamics and Earthquake Engineering*, vol. 26, no. 10, pp. 909–921, 2006.

[13] H. Kawabe and K. Kamae, *Long Period Ground Motion Prediction of Linked Tonankai and Nankai Subduction Earthquakes Using 3D Finite Difference Method*, AGU Fall Meeting, San Francisco, CA, USA, 2005.

[14] S. Aoi and H. Fujiwara, "3D finite difference method using discontinuous grids," *Bulletin of the Seismological Society of America*, vol. 89, no. 4, pp. 918–930, 1999.

[15] A. Salemi, R. Mikaeil, and S. S. Haghshenas, "Integration of finite difference method and genetic algorithm to seismic analysis of circular shallow tunnels (case study: tabriz urban railway tunnels)," *KSCE Journal of Civil Engineering*, vol. 22, no. 5, pp. 1978–1990, 2017.

[16] J. E. Luco and F. C. P. D. Barros, "Dynamic displacements and stresses in the vicinity of a cylindrical cavity embedded in a half space," *Earthquake Engineering and Structural Dynamics*, vol. 23, no. 3, pp. 321–340, 2010.

[17] A. A. Stamos and D. E. Beskos, "3-D seismic response analysis of long lined tunnels in half-space," *Soil Dynamics and Earthquake Engineering*, vol. 15, no. 2, pp. 111–118, 1996.

[18] H. Alielahi, M. Kamalian, and M. Adampira, "Seismic ground amplification by unlined tunnels subjected to vertically propagating SV and P waves using BEM," *Soil Dynamics and Earthquake Engineering*, vol. 71, pp. 63–79, 2015.

[19] H. Alielahi and M. Adampira, "Seismic effects of two-dimensional subsurface cavity on the ground motion by bem: amplification patterns and engineering applications," *International Journal of Civil Engineering*, vol. 14, no. 4, pp. 233–251, 2016.

[20] Z. X. Liu, J. W. Liang, and H. Zhang, "Scattering of plane P and SV waves by a lined tunnel in elastic half space (i): method," *Journal of Natural Disasters*, vol. 19, no. 4, pp. 71–76, 2010.

[21] M. Bouchon, C. A. Schultz, and M. N. ToksÖ, "A fast implementation of boundary integral equation methods to calculate the propagation of seismic waves in laterally varying layered media," *Bulletin of the Seismological Society of America*, vol. 85, no. 6, pp. 1679–1687, 1995.

[22] M. Bouchon, M. Campillo, and S. Gaffet, "A boundary integral equation-discrete wavenumber representation method to study wave propagation in multilayered media having irregular interfaces," *Geophysics*, vol. 54, no. 9, pp. 1134–1140, 2012.

[23] J. Liang and Z. Liu, "Diffraction of plane P waves by a canyon of arbitrary shape in poroelastic half-space (i): formulation," *Earthquake Science*, vol. 22, no. 3, pp. 215–222, 2009.

[24] C. Yi, P. Zhang, D. Johansson, and U. Nyberg, "Dynamic response of a circular lined tunnel with an imperfect interface

subjected to cylindrical P-waves," *Computers and Geotechnics*, vol. 55, no. 1, pp. 165–171, 2014.

[25] X.-Q. Fang and H.-X. Jin, "Visco-elastic imperfect bonding effect on dynamic response of a non-circular lined tunnel subjected to P and SV waves," *Soil Dynamics and Earthquake Engineering*, vol. 88, pp. 1–7, 2016.

[26] X.-Q. Fang and H.-X. Jin, "Dynamic response of a non-circular lined tunnel with visco-elastic imperfect interface in the saturated poroelastic medium," *Computers and Geotechnics*, vol. 83, pp. 98–105, 2017.

[27] G. Ping, Z. Lv, Q. Yan, and H. E. Chuan, "Internal force solution for a deep-buried shield tunnel under the action of a seismic wave," *Modern Tunnelling Technology*, vol. 53, no. 1, pp. 45–51, 2016.

[28] E. Debiasi, A. Gajo, and D. Zonta, "On the seismic response of shallow-buried rectangular structures," *Tunnelling and Underground Space Technology*, vol. 38, pp. 99–113, 2013.

[29] C. Yi, D. Johansson, and U. Nyberg, "Scattering of SH-waves by a shallow circular lined tunnel with an imperfect interface," in *Proceedings of 8th International Symposium on Ground Support in Mining and Underground Construction*, E. Nordlund, T. H. Jones, and A. Eitzenberger, Eds., Luleå, Sweden, September 2016.

[30] X.-Q. Fang, T.-F. Zhang, and H.-Y. Li, "Elastic-slip interface effect on dynamic response of a lined tunnel in a semi-infinite alluvial valley under sh waves," *Tunnelling and Underground Space Technology*, vol. 74, pp. 96–106, 2018.

[31] F. C. P. D. Barros and J. E. Luco, "Diffraction of obliquely incident waves by a cylindrical cavity embedded in a layered viscoelastic half-space," *Soil Dynamics and Earthquake Engineering*, vol. 12, no. 3, pp. 159–171, 1993.

[32] Z. Liu, X. Ju, C. Wu, and J. Liang, "Scattering of plane P 1 waves and dynamic stress concentration by a lined tunnel in a fluid-saturated poroelastic half-space," *Tunnelling and Underground Space Technology*, vol. 67, pp. 71–84, 2017.

[33] C. Smerzini, J. Avilés, R. Paolucci, and F. J. Sánchez-Sesma, "Effect of underground cavities on surface earthquake ground motion under SH wave propagation," *Earthquake Engineering and Structural Dynamics*, vol. 38, no. 12, pp. 1441–1460, 2010.